Blast Wave Loading Pathways in Heterogeneous Material Systems–Experimental and Numerical Approaches

Veera Selvan
Graduate Research Assistant
e-mail: veera_1431@yahoo.co.in

Shailesh Ganpule
Graduate Research Assistant
e-mail: shailesh@huskers.unl.edu

Nick Kleinschmit
Graduate Research Assistant
e-mail: n_kleinschmit@yahoo.com

Namas Chandra[1]
Professor
Fellow, ASME
e-mail: nchandra2@unl.edu

Department of Mechanical
and Materials Engineering,
University of Nebraska-Lincoln,
Lincoln, NE 68588-0656

Blast waves generated in the field explosions impinge on the head-brain complex and induce mechanical pressure pulses in the brain resulting in traumatic brain injury. Severity of the brain injury (mild to moderate to severe) is dependent upon the magnitude and duration of the pressure pulse, which in turn depends on the intensity and duration of the oncoming blast wave. A fluid-filled cylinder is idealized to represent the head-brain complex in its simplest form; the cylinder is experimentally subjected to an air blast of Friedlander type, and the temporal variations of cylinder surface pressures and strains and fluid pressures are measured. Based on these measured data and results from computational simulations, the mechanical loading pathways from the external blast to the pressure field in the fluid are identified; it is hypothesized that the net loading at a given material point in the fluid comprises direct transmissive loads and deflection-induced indirect loads. Parametric studies show that the acoustic impedance mismatches between the cylinder and the contained fluid as well as the flexural rigidity of the cylinder determine the shape/intensity of pressure pulses in the fluid. [DOI: 10.1115/1.4024132]

Keywords: blast wave, pressure, transmission, deflection, impedance, shell thickness

1 Introduction

Improvised explosive devices (IEDs) are weapons frequently used by insurgents in Iraq and Afghanistan; blast waves generated from these IEDs cause traumatic brain injury (TBI), recognized as the "signature wound" in these conflicts. Several theories have been proposed as potential mechanisms of the blast induced traumatic brain injury (bTBI). These theories include vascular transmission [1–6]; direct transmission of the blast wave through cranium [7–14]; flexure of skull [15–17]. The 15-point Glasgow Coma Scale defines the severity of injury as mild (13–15), moderate (9–12), severe (3–8), and vegetative states (<3) [18]. In mild to moderate cases of bTBI, there is no skull fracture; other pathophysiological markers in the brain are well below the detectable levels based on the capabilities of current neuro-imaging or serum biomarkers. This paper addresses the biomechanical loading in these cases, where stresses in the brain results from blast wave-head interactions. Currently, this is achieved through animal models [16,19], post mortem human subjects (PMHS) [20], head surrogates [21–23] and *in vitro* injury models of single cells to 3D cultures [24,25]. Animal and PMHS studies are costly, time consuming and limited to certain lower order animals due to ethical reasons [16,26]. The data interpretation of such studies becomes difficult due to numerous complexities involved (e.g., complexity of head brain parenchyma, challenges associated with the sensor mounting). In addition, scaling/translating animal results to human is a challenging task. The blast wave-head interaction is a complex high rate flow phenomenon and is affected by the oncoming blast wave parameters as well as the geometric and anatomical details of the human head. Thus there is a need for more advanced physical and computational biofidelic models with injury predictive capabilities to complement other direct TBI studies.

Surrogate heads are compatible models to study fundamental aspects of bTBI and to establish critical causative factors; they are easy to build and test. In addition, models can be designed and tested to validate specific hypothesis. An egg shaped skull/brain surrogate model was developed for the study of head response at different orientations during blast loading [21]; spherical surrogate was developed for the study of effects of skull opening for bTBI [22]. In this study, head (skull-brain complex) is idealized as a fluid filled circular cylinder with the longitudinal axis normal to the blast wave propagation. Brain is idealized as fluid contained in the cylinder, the latter being idealized as skull. Top and bottom of the cylinder is allowed to move freely to avoid bending along the axis during blast wave interaction and thus represents a two-dimensional analog of the skull-brain complex.

The overall goal of this paper is to understand the time-dependent spatial variation of the pressure field in the fluid when a fluid-filled cylinder is subjected to an external blast load. In Sec. 2, a theoretical framework for the blast loading of the skull-brain is developed in terms of a cylinder filled with fluid. In this section, a description about the experimental test configurations and the shock tube employed for generating idealized primary blast loading conditions are given. Description about the finite element method used to interpret the experimental data, which is later used to understand the effects of geometric and material parameters of the cylinder on the spatio-temporal evolution of pressure in the fluid is provided. In Sec. 3, the results of the experimental and numerical analysis are presented. Finally, in Sec. 4, the implications of experimental and computational results are discussed in terms of the relationship between pressure field in the fluid (brain), blast characteristics and geometric and material characteristics of the cylinder (head).

2 Methods

Primary blast induced neurotrauma (BINT) is a closed head injury model; when the blast wave interacts with the head, the skull deflects but does not fracture, whereas the brain is injured when the state of stress, strain and/or energy exceeds some critical

---

values. Shape (impulse) of the pressure profile [10,27], oscillatory pressure pulse [28] and focal magnitude of pressure [29] at the neuronal level have all been identified as possible causes of the injury. Hence the effect of blast wave on time-dependent pressure variation in the fluid at any given region needs to be understood in terms of the loading pathways and thus forms the main purpose of the paper.

2.1 Theoretical Considerations. In Sec. 2.1, a theoretical model of a blast wave interacting with a fluid-filled cylinder is developed. The blast wave flow field is described in terms of velocity and pressure as it traverses around the cylinder. The effect of this external blast pressure field on the stress wave and deflection experienced by the cylinder is then illustrated. These effects are then related to the fluid pressure field. It is postulated that the loading at any given point in the fluid can be divided into two separable parts as direct and indirect loading components.

Consider a fluid-filled cylinder subjected to a blast wave, as shown in Fig. 1. The pressure-time relationship of an idealized Friedlander incident wave can be written as

$$p(t) = p^* \left(1 - \frac{t}{t^*}\right) e^{\frac{-bt}{t^*}} \tag{1}$$

where $p(t)$ is the blast wave pressure at any time t at a given point, p^* is the peak overpressure, t^* is the positive duration of a blast wave and b is the decay constant. In actual explosions, the waveforms are more complex due to reflections from ground, structures, debris and enclosures. However, for the sake of standardization, basic studies and comparisons to idealized Friedlander waveform given in Eq. (1) is oftentimes preferred. A generic blast wave comprises a shock front traveling with a Mach number >1 (supersonic), followed by an exponentially decaying blast wind [30]. Without loss of generality, this shock front-blast wind will be referred as the blast wave in this work. In a typical blast wave

of interest, the peak overpressure p^* will be in the range of 3–4 atmospheres (0.2 to 0.3 MPa peak overpressure), with a very sharp rise time in the range of 1 or 2 μs (microsecond) and a total duration of 5–7 ms (millisecond). Based on these parameters, the air shock travels at a velocity of about 500 m/s and the total width of the blast wave is about 2.5 m. Compare this to total impact duration of 10–30 ms for the blunt impact with a much slower rise time [31]. As the blast encounters the fluid-filled cylinder, the mechanical pressure loading pdA occurs based on the total projected surface area of the cylinder. The loading vanishes as the external pressure reduces and lasts only for a few milliseconds concurrent with the blast wave. For example, if the diameter (d) of the cylinder is 50 mm and the shock front velocity (v) is 500 m/s then the travel time past the cylinder is of the order of 0.1 ms. When the same shock front travels across a human head with approximate breadth (b) of 142 mm (5.6″) and length (l) of 183 mm (7.2″), then the travel time is of the order of 0.28 ms to 0.36 ms. As this travel time is very short, the differential pressure experienced by the whole head is significantly lower (differential pressure of 60 kPa for an incident overpressure of 150 kPa).

Given this blast loading condition on a fluid-filled cylinder, we are interested in the state of stress at any given material point in the fluid. When we refer to the state of stress in the fluid, we primarily refer to the hydrostatic compressive stress (pressure) and use these terms interchangeably. Let $P_{\Omega2}(t)$ indicate the state of pressure at any arbitrary point in the fluid, and it varies with time. Thus we seek to evaluate the spatio-temporal variations of $P_{\Omega2}$ given the entire history of blast wave going past the cylinder. A solid body of the cylinder is designated as Ω_1 and the fluid is designated as Ω_2 with the system $\Omega = \Omega_1 \cup \Omega_2$. For the purpose of categorizing the loading pathway, total loading at a given point in the fluid is partitioned into direct and indirect components, such that

$$P_{\Omega2} = P_d + P_{id} \tag{2}$$
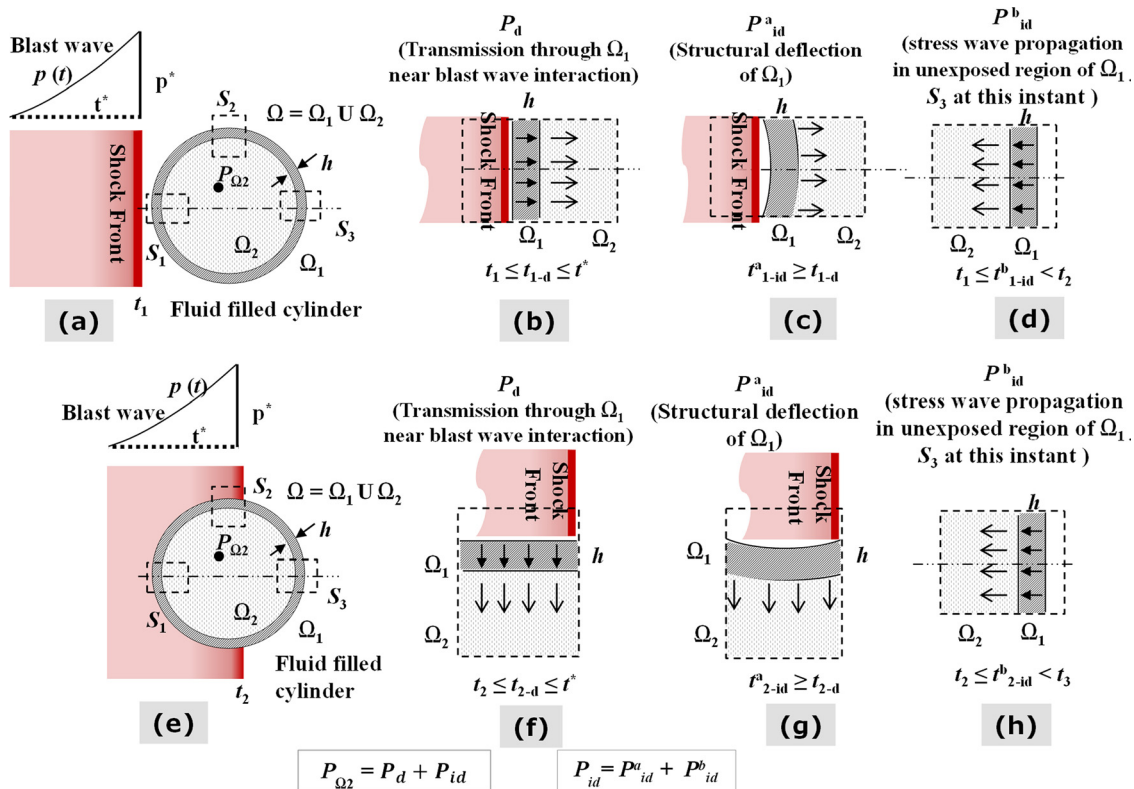
Fig. 1 Blast wave interaction with heterogeneous body: (*a*) and (*e*) are the schematic diagrams of the loading; (*b*) and (*f*) are direct loadings; (*c*), (*d*), (*g*), (*h*) are indirect loadings

where P_d is the direct loading (direct transmission of stress waves in the region of blast wave interaction) and P_{id} is the indirect loading (esp. deflection of the shell) as shown in Fig. 1. Figures 1(a)–1(d) illustrate the initial stages of blast loading on the cylindrical system. Blast wave transmission to the fluid is shown in Fig. 1(b). Blast wave transmission at section S_1 depends on the intensity of blast load at the section and the acoustic impedance mismatch between the cylinder-fluid interface [32,33]. External blast load $F(t)$ at any time t is given by

$$F(t) = \int p_R(t) dA \qquad (3)$$

where $p_R(t)$ is the reflected overpressure of blast wave acting on area dA of section S_1. $p_R(t)$ is generally higher than the incident pressure $p(t)$; this is an important aspect of the problem and will be discussed in detail later. This blast load induces intensive compressive stress waves in the body Ω_1. A fraction of this compressive wave is transmitted to the fluid Ω_2. Intensity of stress transmitted (σ_t) to the fluid can be assumed by the following one dimensional expression

$$\sigma_t = \sigma_i \left(\frac{2Z_{\Omega 2}}{Z_{\Omega 1} + Z_{\Omega 2}} \right) \qquad (4)$$

where $Z_{\Omega 1} = \rho_{\Omega 1} c_{\Omega 1}$ and $Z_{\Omega 2} = \rho_{\Omega 2} c_{\Omega 2}$ are the impedance of body Ω_1 and fluid Ω_2, respectively, σ_i is the intensity of incident wave on the interface and ρ and c are the density and acoustic velocity of the medium. Thus the magnitude of direct loading as seen in Fig. 1(b) depends on the blast load and the material properties; it continuously varies as the blast wave is unloaded as given by Eq. (1). It should be noted that the Eq. (4) is based on one dimensional theory, and is not strictly valid for cylindrical solutions. This equation is employed to explain the loading pathway at the section level (say S_1). This equation should be viewed and used with limitations for three dimensional problems.

Apart from direct transmission as shown in Fig. 1(b) the cylindrical structure gets loaded, which in turn causes not only local deflection as seen in Fig. 1(c) but also a global deflection as the generated stress waves propagate in both directions. This local deflection due to the stress wave propagation interacts with the fluid which is the indirect component of the loading; the magnitude of the indirect load depends on the geometric and material properties of the cylinder. For instance the local displacement of a circular ring subjected to an applied concentrated load F is given by

$$\delta \propto \frac{FR^3}{EI} \qquad (5)$$

where R is the mean radius of the cylinder, and E is the young's modulus and I is the area moment of inertia of the ring [34]. It can thus be seen that deflection decreases as the flexural rigidity is increased or the radius is decreased when all other factors are kept constant. Typical longitudinal stress wave speeds in the solid material are higher than the air shock velocity. For example, stress wave travels at 2270, 5960, and 2900 m/s in polycarbonate, steel, and skull respectively which are much higher than the typical air shock velocity of 500 m/s. Hence, stress wave travels faster in the cylinder, loads the fluid much before the arrival of the shock front as is seen in Fig. 1(d). This stress wave propagation pattern causes a tensile state of stress leading to possible cavitation, depending on the magnitude of the stress vis-à-vis the vapor pressure of the fluid. Thus, a typical material point $P_{\Omega 2}$ is stressed from both direct and indirect loadings.

Figures 1(e)–1(h) depict the blast-structure-fluid interaction at a point of time when the shock front passes the midpoint of the cylinder in region S_2. In this case, the direct loading occurs in the region S_2 while the stress wave propagates from S_2 to both the

sides of the cylinders. As the stress waves travel from these instantaneous loading regions, they superimpose on stress waves arriving due to previous loadings; see for example Figs. 1(b) to 1(d). Thus, a very complex set of loading pattern emerges affecting the pressure at $P_{\Omega 2}$. Hence, total load at point $P_{\Omega 2}$ in the fluid is a combination of direct and indirect loads emerging at various sections of the body. Though peak values of pressures usually occur when the direct and indirect loads are both actively loading a point, this is not always the case. Though the direct load disappears when the tail of the blast wave is past the entire cylinder, indirect load due to already distorted cylinder persists until all the elastic energy is dissipated in the fluid as well as the cylinder.

2.2 Experiments. The surrogate head model used in the study is subjected to planar blast waves of the Friedlander type in a specially designed shock tube. A 229 mm × 229 mm steel square compression driven shock tube has been designed and tested at the University of Nebraska Lincoln's (UNL) shock wave generation facility [35]. This shock tube consists of three main sections—cylindrical driver section, square driven section and a transition section between the driver and driven. The driver section contains pressurized gas (e.g., Nitrogen or Helium) which is separated from the transition by several 0.025 mm thick Mylar membranes, while the remaining sections contain air at atmospheric pressure and temperature. Cross sectional transition from circular driver to square driven is achieved with the transition section. Upon membrane rupture a blast wave is generated which expands through the transition and develops into a planar blast wave in the driven section. Test section (which is part of driven section) is strategically located to expose specimens to the blast wave profile of interest. A high speed video camera (600,000 frames per second) is placed near the test section to capture the blast-specimen interaction events. The shock tube is designed and built such that a fully developed planar blast wave is obtained in the test section located approximately 2502 mm from the driver end; total length of the shock tube is 12,319 mm. The test location can be varied depending on the desired peak overpressure, positive duration and impulse, which in turn depend on the strength of the explosive and standoff distance of the specimen from the explosive.

A cylindrical head model (diameter 50 mm, thickness 2 mm, and length 178 mm) is developed with a polycarbonate cylinder filled with mineral oil. The material of the cylindrical shell and fluid are selected such that they closely mimic the human skull and the brain respectively in terms of density and acoustic wave speed. Mineral oil is chosen over water to reduce cavitation effects. The cylinder is mounted on sliders, as shown in Fig. 2 so that the cylinder can easily slide (translate); this is important to eliminate bending (end) effects that might occur if the cylinder were to be rigidly mounted. In addition, this freedom to slide is more representative of free-field blast loading experienced by a dismounted soldier.

The response of the cylindrical shell to the blast wave is measured with surface pressure and surface strain gauges; response of fluid is monitored with pressure sensors at different points within the fluid. The sensor configuration consists of a surface mounted pressure sensors (Kulite model LE-080-250 A) and circumferentially mounted Vishay strain gauges (model CEA-13-250UN-350) located at 0 deg (F1), 90 deg (M1), and 180 deg (B1) with respect to the oncoming shock wave. Strain gauges are glued circumferentially on the cylinder surface using M-bond adhesive and they measure circumferential strain. Surface pressure sensors are glued and taped using rubber cement and duct tape with the sensing surface exposed. Surface pressure sensors measure the reflected blast overpressures, record the arrival of blast waves and track their flow. Probe-style Kulite pressure sensors (model XCL-072-500 A) that measure the fluid pressures are mounted at the center (M2) of the tube as well as at offsets of 19 mm in front of (F2) and behind (B2) the center sensor, as shown in Fig. 3. These sensors are
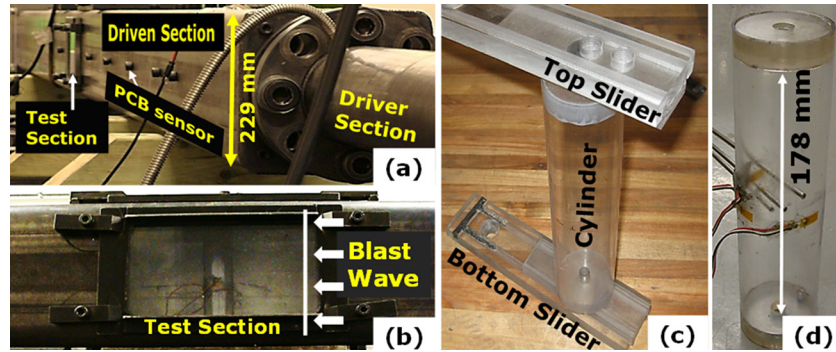
Fig. 2 (*a*) A 229 mm × 229 mm steel square-12 m long shock tube used in the experiments; (*b*) Fluid-filled cylinder inside the test section; (*c*) Cylindrical system with top and bottom sliders; (*d*) Cylinder (without fluid for clarity) showing the surface mount pressure/strain gauges on the cylinders and pressure probe mounts in the fluid
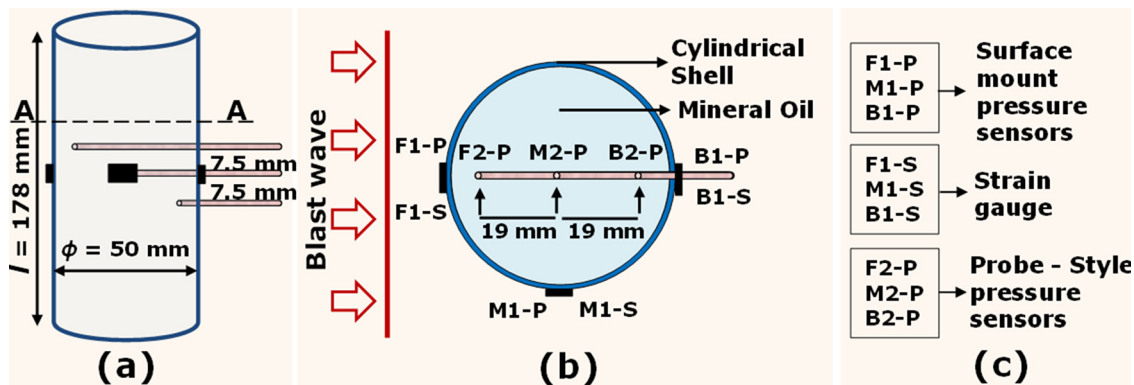

Fig. 3 (*a*) Schematics of the experimental cylindrical setup; (*b*) Sectional view A-A showing all the sensor locations (*c*) Sensor type/location terminology: First letter-F=front, M=middle, B=back; Second number-1=outside, 2=inside; Third letter-P=air surface pressure or fluid probe pressure, S=surface mounted strain gauge

mounted inside the cylinder at an orientation perpendicular to the oncoming shock front. The three sensors are vertically aligned 7.5 mm apart with the middle sensor being mounted in the middle of the tube. Figure 3 shows the sensor configuration.

The sensing elements can measure the absolute pressure from 0–1.72 MPa (0–250 psi) with a nominal calibration of 58.02 mV/MPa (0.400 mV/psi) using 10 Vs excitation. All pressure sensors used in the experiments are calibrated under shock/dynamic loading conditions using a separate 101 mm (4″) diameter shock tube. Accurate calibrations are achieved by generating precisely controlled blast wave velocities and invoking the Rankine-Hugoniot jump conditions to relate the blast wave velocity to blast wave overpressures. The data acquisition time interval in the experiment is 1 μs (microsecond). Each set of experiments reported in this paper is repeated at least three times ($n = 3$). However, plots are used from a single experiment.

2.3 Computational Model. The primary purpose of the computational model is to understand the dynamics of blast loading at given shell and fluid points. Blast structure interaction is a short dynamic event and hence the explicit dynamic analysis is employed to simulate the event. Interaction between blast wave and structure is enabled by coupled Eulerian-Lagrangian (CEL) technique. Simulated results are then compared against experimental results for the validation of the developed numerical model.

2.3.1 FE Discretization. Finite element (FE) modeling technique is used to simulate the propagation of a planar blast wave

through the shock tube and its interaction with the cylinder. The cylinder and the fluid contained in it are modeled with Lagrangian elements. The air inside the shock tube is modeled with Eulerian elements. Schematic of the setup is shown in Fig. 4(*a*). Eulerian framework allows modeling of highly dynamic events (e.g., shock) which will otherwise induce heavy mesh distortion. This approach has been used in the past by various researchers [26,36–41]. Lagrangian and Eulerian domains are meshed with 8 node brick element. Interaction between the cylindrical shell and the fluid is modeled through tied (no sliding, no separation) contact. No separation behavior is necessary to simulate countercoup phenomena typically observed in head injuries. No separation allows tensile loads to be transferred across the interface.

An enhanced immersed boundary method is used to provide the coupling between Eulerian and Lagrangian domains. Interaction between the propagating blast wave and cylindrical shell is defined through a "general contact" feature (card) in ABAQUS®. In general contact, contact constraints are enforced through penalty method with finite sliding contact formulation. Various contact property models are available in general contact. In the present work, frictionless tangential sliding with hard contact is used as a contact property model. Hard contact defines pressure-overclosure relationship between contacting surfaces. Hard contact behavior implies that: (1) the surfaces transmit no contact pressure unless the nodes of the slave surface contact the master surface (2) no penetration is allowed at each constraint location and (3) there is no limit to the magnitude of contact pressure that can be transmitted when the surfaces are in contact. Mesh convergence studies have been performed for both Eulerian and
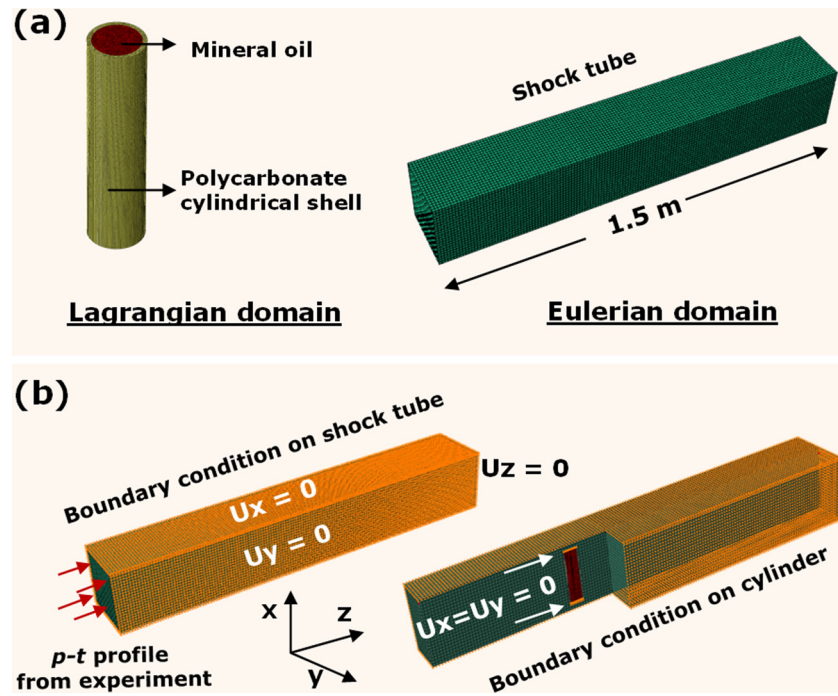
Fig. 4 (*a*) FE discretization; (*b*) Loading and boundary conditions employed in the simulation

Table 1 Finite element discretization

Model	Domain	No. of nodes	No. of elements	Type of element
Air	Eulerian	1,357,360	1,316,250	Hexahedral
Polycarbonate cylinder	Lagrangian	95,823	66,740	Hexahedral
Mineral oil	Lagrangian	409,752	393,860	Hexahedral

Lagrangian elements. The mesh convergence criterion is based on less than 5% change in the peak value of a given field variable (i.e., reflected overpressure, shell strain and fluid pressure). Mesh convergence is achieved at element sizes of 3 mm, 1 mm, and 1 mm, respectively, for air, cylindrical shell and fluid inside the cylinder. Table 1 shows the number of nodes, number of elements, and element types for each component of the converged FE model.

2.3.2 Material Models. Air is modeled as an ideal gas equation of state (EOS) given by

$$P = (\gamma - 1)\frac{\rho}{\rho_0}e \qquad (6)$$

where P is the pressure, γ is the specific heat ratio (1.4 for air), ρ_0 is the initial air mass density and ρ is the current mass density and e is the internal volumetric energy density. Mach number of the shock front obtained from our experiments is approximately 1.5; hence the ideal gas EOS assumption is acceptable as the ratio of specific heats does not change drastically at this Mach number. The cylindrical shell is modeled as linear, elastic, isotropic solid with the material properties of polycarbonate (base case) and steel (parametric studies). The shell strains obtained from the experiments are less than 1%; hence linear, elastic modeling assumption is valid. The fluid contained in the cylinder is modeled with Mie-Gruneisen EOS that relates the final state of density (ρ) to corresponding pressure and is given by

$$P_H = \frac{\rho_0 C_0^2 \eta}{[1 - s\eta]^2} \qquad (7)$$

where, P_H is the hugoniot pressure, ρ_0 is the reference density, C_0 is the reference wave speed, $\eta = [1 - (\rho_o/\rho)]$ is the nominal volumetric compressive strain, and $s = dU_s/dU_p$ is the linear Hugoniot slope coefficient. Material properties of polycarbonate and mineral oil are close to the material properties of the skull and brain respectively [42,43]. Material properties are listed in Table 2.

2.3.3 Loading and Boundary Condition. Experimental pressure boundary condition (i.e., experimentally measured pressure-time (p-t) profile deep inside the shock tube) is used as an input for the FE simulations. Displacement perpendicular to the faces of the shock tube is kept zero in order to avoid escaping/leaking of air through these faces as shown in Fig. 4(*b*). Hence, there would be no lateral flow during shock wave propagation. Top and bottom faces of the cylindrical model are constrained in the vertical and transverse directions; the cylinder can move freely (frictionless) along the direction of blast wave propagation. It should be noted that probe holders that hold the sensors are not included in the modeling. Simulations with the probe holders are carried out in pilot studies and it is found that the probe holders do not have a significant effect on the wave propagation inside the fluid.

2.3.4 Solution Scheme. The finite element model is solved using a nonlinear transient dynamic procedure with CEL method (ABAQUS®). This approach is validated against known analytical solutions. In addition, further validation of Fluid structure Interaction (FSI) modeling using ABAQUS® can be found in Mougeotte et al. [44]. In this approach, the governing partial differential equations for conservation of momentum, mass and energy along with material constitutive equations and equations defining the initial and the boundary conditions are solved simultaneously. In

Table 2 Material properties

Material	Density (kg/m^3)	Elastic/Bulk^a Modulus (MPa)	Poisson's ratio	Speed of sound (m/s)	Temperature (K)	Gas constant (J/kg-K)
Skull	1710	5370	0.19	2900	—	—
Polycarbonate	1220	2380	0.37	2270	—	—
Brain	1040	2190^a	—	1509	—	—
Mineral oil	825	1600^a	—	1440	—	—
Water	1000	2400^a	—	1482	—	—
Steel	7880	200000	0.3	5960	—	—
Air	1.2	—	—	347	300	287

ABAQUS$^®$ the Eulerian time incrementation algorithm is based on an operator split of the governing equations, resulting in a traditional Lagrangian phase followed by an Eulerian phase. During the Lagrangian phase of the time increment, nodes are assumed to be temporarily fixed within the material and the elements deform with the material. During Eulerian phase of the time increment, deformation is suspended, elements with significant deformation are automatically remeshed, and the corresponding material flow between neighboring elements is computed. As material flows through an Eulerian mesh, state variables are transferred between elements by advection. In the current analysis, 8 node brick elements are employed which use isoparametric interpolation functions.

An enhanced immersed boundary method is used to provide the coupling between Eulerian and Lagrangian domains. Here, Lagrangian region resides fully or partially within Eulerian region and provides no-flow boundary conditions to the fluid in the direction normal to the local surface. Further, Eulerian region provides the pressure boundary conditions to the Lagrangian region. Thus a combination of fixed Eulerian mesh and solid-fluid interface modeling through enhanced immersed boundary method allows for concurrent simulations of the formation and propagation of primary shock wave in a fluid medium and accounts for the FSI effects and structural deformations once the shockwave encounters a solid.

In CEL, the whole model is solved using the same Lagrangian equations. For the Eulerian part/domain in the model the results are simply mapped back to the original mesh. The Lagrangian (solid) body can be a deformable body and can deform based on the forces acting on it and the deformation of the Lagrangian solid influences the Eulerian part/domain. For the current analysis, a typical simulation requires about 24 hs of CPU time on 8 dedicated Opteron parallel processors (processor speed 2.2 GHz, 2 GB memory per processor), for an integration time of 2.5 ms for a single run. In this work, automatic time stepping is used with explicit central-difference time integration. In automatic time stepping, time increment $(=\sqrt{L_{min}/C})$ is calculated at each increment for each element based on element size and wave speed. This calculation resulted in the time step of 8.7 e–8 s for the simulations.

3 Results

As outlined in the theoretical considerations, pressure-time variations at a given material point in the fluid are resultants of the instantaneous effects of direct and indirect loads arriving at that point. Both these loads emanating from different sources vary in magnitude and arrive at a given point from different directions. Thus, the propagation process is quite complex. Only some selected features of the measured (or computed) pulse at a given point, e.g., arrival time and initial peak are typically traceable. The results in Sec. 1, relates experimental measurements (Fig. 5) to numerical results (Figs. 6–8) for the purposes of model validation. It should be noted that for this set of the results, experiments and simulations are carried out on 2 mm thick polycarbonate shell filled with the mineral oil. The second section (Figs. 9–13) shows the parametric studies carried out to understand different loading pathways, which are addressed in detail in Sec. 4. The measurements are discussed in terms of the reflected blast overpressure

and strain fields in the cylindrical shell and pressure fields in the fluid.

3.1 Experimental Results. Table 3 shows the experimentally measured arrival times and corresponding calculated velocities at all sensor locations. Row 1 gives the arrival time and row 2 gives the distance traveled by the wave between sensors. The calculated velocities are shown in row 3. Wave velocities are calculated based on the distance between the sensors and differences in arrival time. Arc length of the shell is used to calculate wave velocity in the shell whereas to calculate wave velocity in air and the fluid, direct distance (longitudinal) between the sensors is used. Blast wave velocities vary on the surface of the cylinder whereas the velocities in the shell and mineral oil are close to their longitudinal wave speeds.

Experimentally measured blast overpressures (F1-P, M1-P, B1-P) and longitudinal strains (F1-S, M1-S, B1-S) on the surface of the cylinder, and pressures (F2-P, M2-P, B2-P) in the fluid are shown in Fig. 5. Terminologies used in the designation of these locations are shown in Fig. 3(c). Reflected blast overpressure at the frontal location (F1) shows a very sharp rise followed by a decaying pressure pattern (Fig. 5(b)). The peak overpressure at location F1 is amplified 2.5 times the incident pressure. Peak overpressures at side (M1) and rear (B1) are significantly lower ($\wedge_{M1} = 0.63$ and $\wedge_{B1} = 0.94$) than the reflected overpressure at the front (F1) ($\wedge_{F1} = 2.5$); all three pressure pulses begin to equilibrate after about 4 ms Small secondary peak observed in the pressure profile at $t = 1.6$ ms is due to the side wall reflection from the blast tube. Using numerical simulations, it is found that the secondary reflection has very minimal effects on the pressure pulses observed in the fluid.

Surface mounted strain gauges (F1-S, M1-S and B1-S) measure negative (compressive), positive (tensile) and negative (compressive) strains, respectively as shown in Fig. 5(c). Strain measure indicates that the front section undergoes compression while the middle section is under tension, i.e., the circular cylinder becomes elliptical with major axis passing through M1 and perpendicular to the flow and minor axis passing through F1 and B1. The fluid pressure measured at F2 (Fig. 5(d)) shows a sharp pressure rise followed by pressure decay (till $t = 1.5$ ms). This is attributed to transmission of pressure from the surface (F1-P) to the fluid. After $t = 1.5$ ms the pressure is again increased (secondary rise). This secondary rise is attributed to shell deformation. The pressure eventually dies down at $t = 2.5$ ms. Fluid pressures at M2 and B2 show similar trend but the initial magnitude of peak pressure is reduced as we go from F2-M2-B2. In addition M2 shows significantly higher oscillations as compared to sensor F2 and B2.

3.2 Numerical Model Validation. Figure 6 shows the numerical results of blast overpressures at experimental locations, superimposed with the experimental data for comparison purposes. It should be noted that for ease of comparison, the shock wave arrival times of the simulations are shifted to match the experimental arrival times. Simulated blast overpressures are in good agreement with the experimental data. Simulation is able to capture the main features like shock front, peak pressure, negative phase and secondary rise.
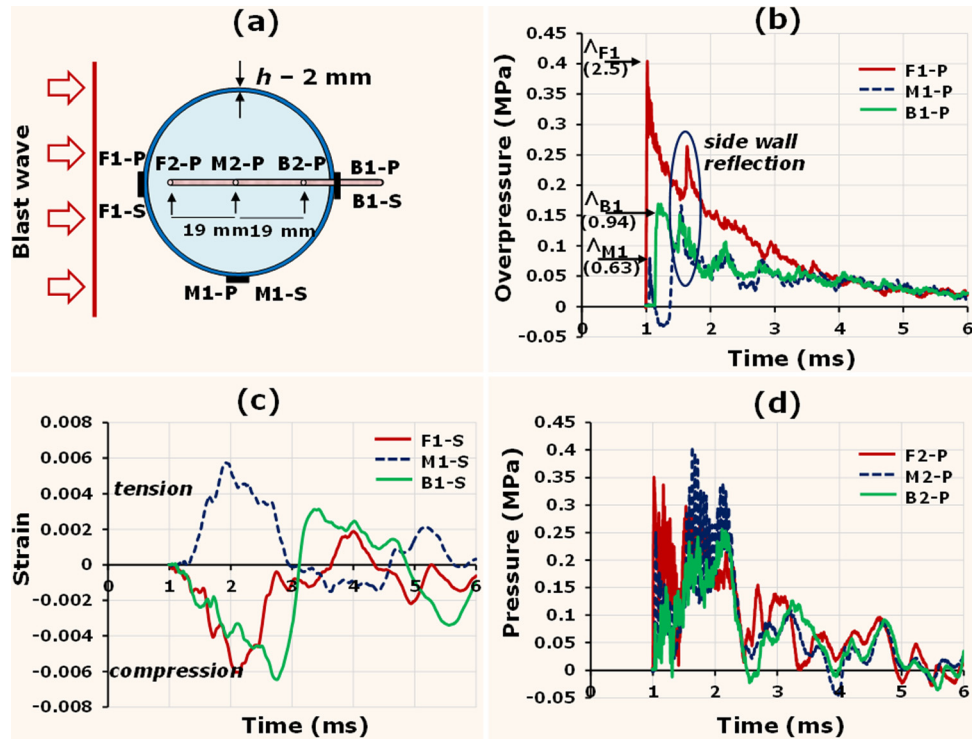
Fig. 5 Experimental measurements at various locations (*a*) schematic view of measurement locations; (*b*) external blast overpressures; (*c*) cylindrical shell strain; (*d*) pressure pulse in the fluid
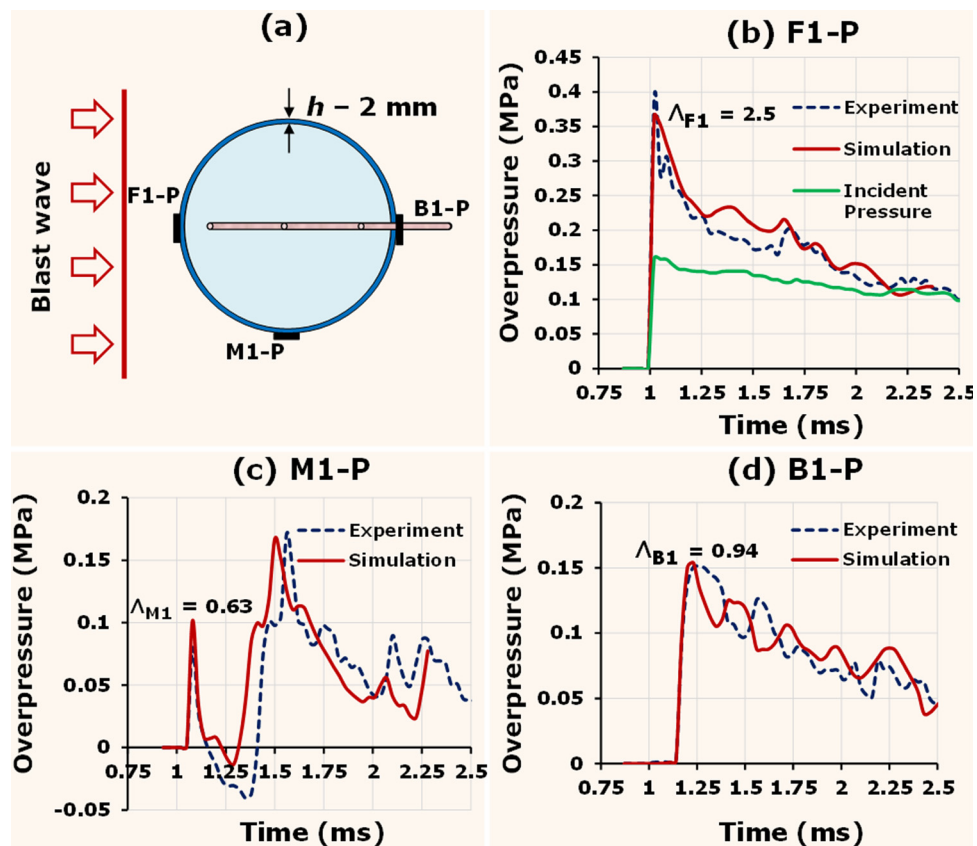

Fig. 6 Comparison of experimental and numerical blast pressures at three locations: (*a*) schematic; (*b*) front; (*c*) middle; (*d*) back

Comparison between experimental and numerical strains at location F1, M1 and B1 are shown in Fig. 7. The simulation results agree with the experimental data and predict the same pattern of compression, tension and compression at locations F1, M1 and B1, respectively. Shape change from circle to ellipse (Fig. 7(a)) is clearly captured in the simulation. Comparison of fluid pressures between the experiment and numerical simulations at location F2, M2 and B2 are shown in Fig. 8. For ease of comparison, pressure profiles obtained from the simulation are filtered at 15 kHz. The simulated pressure profiles show a similar pattern as that of the experiments. At location F2, the sharp pressure rise from the simulation is consistent with the shock front rise time from the experiments. Response of pressure gauge at M2 (geometric center) shows the trend of a pressure pulse superimposed by a periodic oscillation. The period of oscillation corresponds to the round trip travel time of an acoustic stress wave across the interior of the cylinder (23 mm radial distance in 16 μs). At location B2, simulation captures pressure rises due to direct (transmission) and indirect (deflection) loading that is consistent with the experimental results.

Though simulation results match fairly well with the experimental results, some discrepancies in the experimental and simulation data are observed. In the simulations, the shock wave travels faster than the experiments and the difference is of the order of 0.2 ms. This difference in velocity between experiment and simulation is attributed to the ideal gas equation of state modeling assumption, membrane rupture pattern and the friction along the inner wall of the shock tube [21,36,37,39]. However, for ease of comparison between experimental data and simulation results, the shock wave arrival times of the simulations are shifted so that arrival times match with the experiments. It is not only the shock front, but the entire blast wave (including shock foot or tail) travels faster in the simulation. A similar trend is observed in our previous works [36,37,39]. Due to differences in the shock wave velocities though the mismatch between experiments and simulation in the pulse decay region appears to be out of phase, it can be partially attributed to the velocity mismatch. The authors have performed fast fourier transform (FFT) analysis on experimental and computational data. From the FFT analysis, it is seen that the dominant frequencies of the oscillations are similar in the experiments and simulations (for example, dominant frequencies of 1.95 kHz, 2.7 kHz, and 3.7 kHz are seen for sensor F2-P).

3.3 Parametric Studies on Cylindrical Head Model. The results of numerical simulations match the experimental data fairly well; in-depth analyses of the effect of different parameters are provided in this section. Since the pressure field in the fluid is affected by the structural (material/geometry) response of the cylinder, both material and thickness of the cylinder are independently varied for the study.

Effect of material and thickness of the cylinder on fluid pressures are shown in Fig. 9. Two thicknesses (2 and 7 mm) and two materials (polycarbonate and steel) are used in the study. Peak pressures at F2 are reduced as the shell material is changed from polycarbonate to steel. In addition, sensor B2 shows negative pressure (initial pressure rise) in case of steel (Figs. 9(c) and 9(f)), whereas for polycarbonate positive pressure (initial pressure rise) is observed at B2 (Figs. 9(b) and 9(e)). Similarly as the shell thickness is increased from 2 mm to 7 mm the peak pressures are reduced for both polycarbonate (Fig. 9(b) and 9(e)) and steel (Fig. 9(c) and 9(f)). Apart from the magnitude, other patterns in the pressure profiles remain unchanged for 2 mm and 7 mm steel cases as seen in Figs. 9(c) and 9(f). But for polycarbonate case, patterns in the pressure profiles vary substantially between 2 mm and 7 mm as seen in Fig. 9(b) and 9(e).
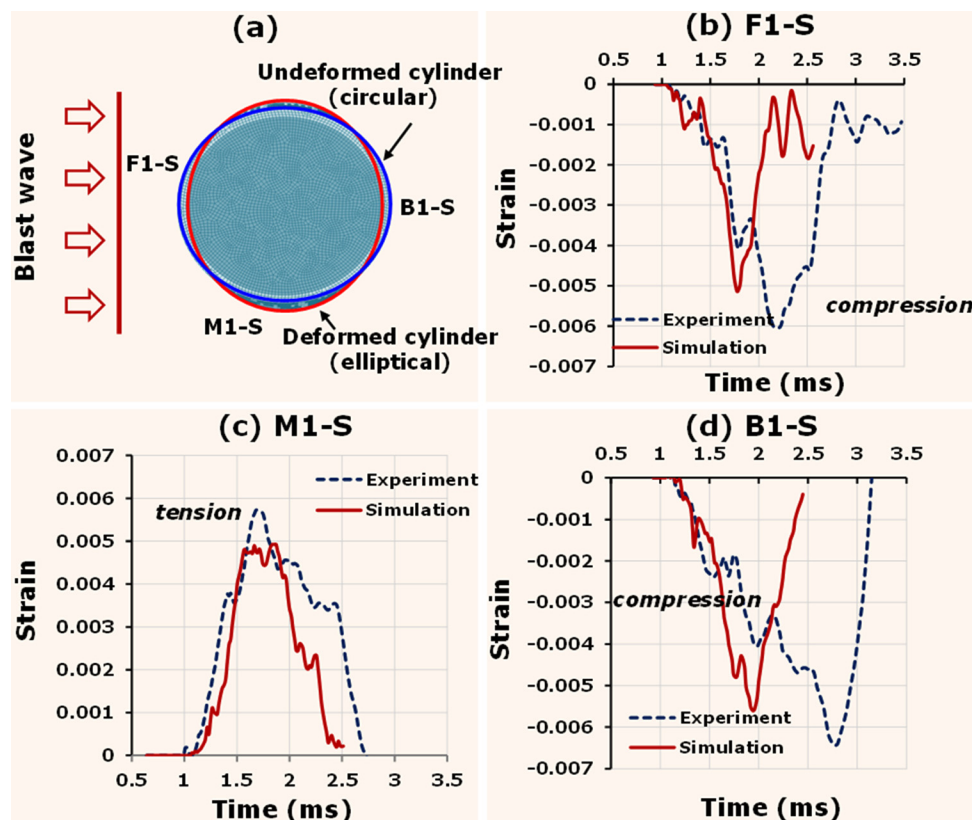

Fig. 7 Comparison of experimental and numerical shell strains at three locations: (a) shape change of the cylinder from circle to ellipse obtained from simulation (b) front; (c) middle; and (d) back
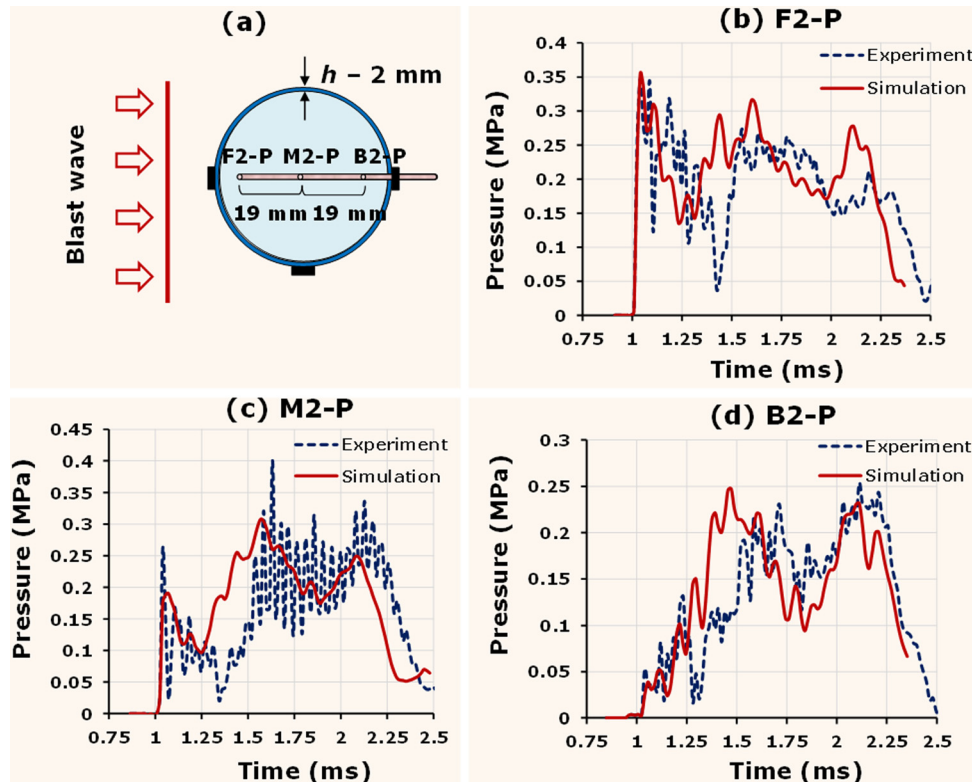
Fig. 8 Comparison of experimental and numerical simulation results at three locations inside the fluid: (*a*) schematics; (*b*) front; (*c*) middle-notice the pressure oscillations (*t*=1.5–2 ms) corresponding to the round trip wave motion; and (*d*) back
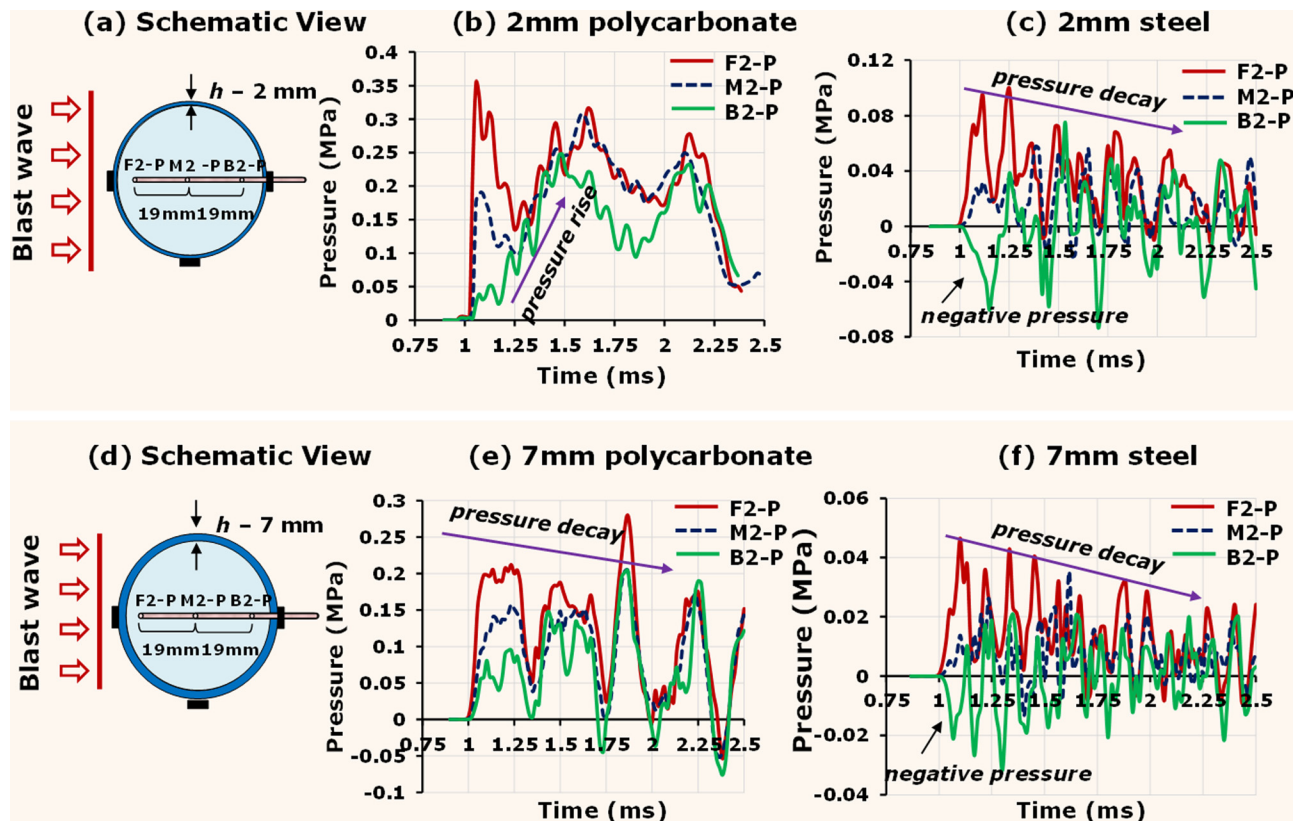

Fig. 9 Numerical simulations of pressure pulse: Top row- 2 mm polycarbonate/steel; Bottom row-7 mm polycarbonate/steel; Pressure rise in (*b*) corresponds to deflection-dominated indirect loads, absent in other cases

4 Discussions

It can be seen from the previous sections that the pressure in the fluid is a complex function of external blast flow dynamics, geometry/material of the cylinder and acoustic velocity of the fluid. In order to fully understand the mechanics of the direct transmissive load and the structural deflection-induced indirect loads, it is important to pare down the sequence of different wave motions arriving at a point, by monitoring the time of arrival of different waves. The very first response of either the external surface pressure, strain, or the internal fluid pressure will indicate the arrival of different waves.

4.1 Arrival Time Analysis. Arrival time analysis of the experimentally measured values in the case of the 2 mm polycarbonate case is shown in Table 3. From the table, it can be seen that the flow velocity around the cylinder between F1 and M1 (anterior to lateral) is 550 m/s and flow velocity between M1 and B1 (lateral to posterior) is 270 m/s. Compare these velocities to the far-field shock velocity of 500 m/s. Hence there is a speed-up from anterior to midpoint (lateral) and slow-down from the midpoint to the posterior location. This speed-up and slow-down process is due to the blast wave and cylinder interaction dynamics (Fig. 10). As the shock front impinges on the cylinder at its most upstream region (see Fig. 1, region S_1), a reflected shock propagating in the opposite direction starts to develop. At the same time, regular reflections occur that propagate radially and in the upstream direction. Thus, a compressive pattern of variable strength develops as a result of incident shock reflection over the surface and upstream motion of the blast wave. At an angle of about 45 deg from the leading-edge radius, Mach reflection takes place. In this region, the shock foot propagates faster than the shock front. At 90 deg, the shock foot has the same speed as the shock front. At angles greater than 90 deg, the shock foot starts to slowdown relative to the shock front resulting in generation of expansion waves. These expansion waves are formed after the shockwave passes the top point of the cylinder at 90 deg from the leading edge. At an angle of 180 deg from the leading edge, blast traversing from the sides of the cylinder meet (flow union) resulting in higher pressure as compared to the pressure at 90 deg. Similar observations are reported by Ofengeim et al. [45].

It is critical to understand the wave propagation in the cylindrical shell and the fluid. Based on the arrival time analysis of strain gauges at F1, M1, and B1, stress wave velocity in the cylindrical shell is 2400 ± 100 m/s (Table 3). This calculated wave velocity is
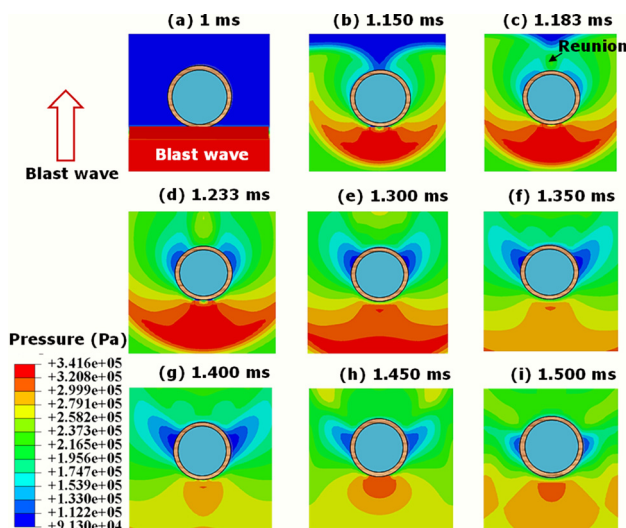

Fig. 10 Numerical simulation of external flow field at different time points: (a) to (c) show the reflected wave fronts moving upstream; (d) to (g) show the evolution of expansion waves

close to the longitudinal wave speed of polycarbonate (2270 m/s). Similarly, calculated wave velocity (1450 ± 110 m/s) in the fluid from the arrival time analysis is close to the longitudinal wave speed of the fluid (1440 m/s).

The arrival of the pressure wave at the front sensor (F2) in the fluid is $6 \mu s$ after the arrival of the surface pressure wave at sensor F1 (Table 3). This indicates that pressure wave in the fluid is due to the direct transmission of the blast wave. Once the wave is initiated in the fluid, it travels at the longitudinal wave speed of the fluid and accounts for the initial sharp pressure rise at sensor M2 and B2.

4.2 Pressure Magnitude

4.2.1 Blast Load. It needs to be recognized that the blast wave is a moving load with the shock front (head of the blast wave) inducing much higher load compared to that of the tail. The magnitude of this moving load inflicted on the structure is primarily determined by the area involved in the blast-structure interaction region and the corresponding reflected blast overpressure at that region as given in Eq. (3). Reflected blast overpressure can be expressed as an amplification ratio of the blast wave and is given by

$$\wedge = \frac{p_R(t)}{p_i(t)} \tag{8}$$

where $p_R(t)$ and $p_i(t)$ are incident and reflected overpressures of a blast wave, respectively. The reflected overpressure range for an air shock is within $2 \le \wedge \le 8$. Value of $\wedge$ depends on (a) the relative orientation of surface normal to the blast wave flow direction, (b) rigidity of surface (yielding or unyielding), (c) velocity of the shock wave (or its Mach number), and (d) geometry, material and stiffness of the object [46].

From the interaction pattern of blast wave with cylinder, it is clear that the blast wave impinges normal to the cylindrical surface in frontal interaction (F1) leading to high $\wedge_{F1}$ ($=2.5$) where both static and dynamic pressures are involved. When the blast wave approaches the sides (M1) the entire front half is engulfed in blast loading with structural loading per unit area (local traction) changing due to two reasons: (i) Reflection ratio ($\wedge$) changes as a function of the angle between the blast propagation direction and the local normal to the surface. At this point, the flow is almost parallel to the sides (M1) and has a minimum value of $\wedge$ since only static pressure is involved in the interaction, and (ii) very presence of the cylinder which changes flow dynamics as blast wave traverses from the front (F1) to sides (M1) (see Fig. 10). At the rear (B1), the blast wave traversing the both sides of the cylinder reunites (Fig. 10(c)) thus leading to higher amplification ($\wedge_{B1}$ (0.94)) compared to the middle ($\wedge_{M1}$ (0.63)). Thus direct load changes around the periphery as the reflection ratio $\wedge$ changes. It turns out that the magnitude of pressure generated in the fluid is highest at the front (F2) and is due the direct transmission of the blast overpressure from the surface (F1).

4.2.2 Impedance Mismatch. The magnitude of the pressure transmitted to the fluid due to blast interaction depends on the reflected pressure and the impedance mismatch. Pressure transmitted to the fluid is assumed by the following expression

$$\sigma_t = \sigma_i \left(\frac{2 Z_{\Omega m}}{Z_{\Omega p} + Z_{\Omega m}} \right) \tag{9}$$

where σ_i is the incident stress wave impinging on the interface between polycarbonate and mineral oil, σ_t is the stress wave transmitted to the mineral oil and $Z_{\Omega m}$ and $Z_{\Omega p}$ are the impedance of mineral oil and polycarbonate, respectively. Steel has a much higher impedance (47 MPa-s/m) compared to polycarbonate (2.76 MPa-s/m) and mineral oil (1.2 MPa-s/m). Based on these impedances, the intensity of stress wave transmitted to the fluid in the polycarbonate case ($\sigma_t = 0. 61\sigma_i$) is higher than the steel case

($\sigma_t = 0.049\sigma_i$). Hence, higher the impedance mismatch, lesser is the transmission [21,23,32]. Thus the magnitude of pressure waves in the fluid for 2 mm steel case is less compared to 2 mm polycarbonate case. As the impedance mismatch determines the magnitude of transmitted waves, it can be concluded that direct load is inversely proportional to impedance mismatch.

4.2.3 Shell Thickness. Figure 9 clearly shows that the pressure transmission reduces with increase in thickness. Though 2 mm and 7 mm polycarbonate cases have the same impedance mismatch, peak pressure in the fluid for 7 mm thick shell is lesser than the 2 mm case. A similar trend is also observed in 2 mm and 7 mm steel cases. Thus, it is clear that the blast wave transmission reduces with increase in shell thickness.

When the cylinder is subjected to shock loading (see Fig. 1, region S_1), there is a direct transmission of stress followed by the indirect loading due to shell deflection. While the direct load is determined by the impedance mismatch condition (acoustic response), the deformation of the cylinder in the vicinity of the loading is determined by the structural response. The structural response is measured in terms of flexure rigidity (EI) where E is the modulus of elasticity and I is moment of inertial. EI not only controls the structural response but also determines the wave speed. For the same diameter of the cylinder, an increase in thickness leads to increase in the moment of inertia, and hence lower deflection. Stress in the fluid arising due to the shell deflection is indirect load; this indirect load is maximum for 2 mm polycarbonate and it reduces for 7 mm polycarbonate. For 2 mm and 7 mm steel cases it still reduces further (Fig. 9). Thus, as the structural rigidity of the cylinder is increased either through an increase in the modulus of elasticity or/and thickness of the shell, indirect load to the fluid decreases.

4.3 Correlation Between Fluid Pressure and Shell Strain. In the previous sections it is shown that an initial pressure rise in the fluid is due to transmission of blast wave to the fluid and is governed by blast wave-cylinder interactions at the anterior portion (see Fig. 1, region S_1) of the cylinder. In this section, the relation between fluid pressure and surface strains is illustrated. Figure 11 compares the (circumferential) strain in the cylinder at side (M1) with the fluid pressure at the center of the cylinder (M2), for 2 mm polycarbonate case. From the figure, it can be seen that the rise and fall of the pressure in the fluid is strongly related to the strain variation in the cylinder. Further, the pressure pulse is a combination of internal wave reflections in fluid and shell deflection (indirect load). This then explains the pressure rise observed in Fig. 9(b) for all the three fluid pressure data. For 7 mm polycarbonate and for both the 2 and 7 mm steel cases shell deflections are limited and hence there is no significant pressure

rise. Thus, pressure decays with time for these cases as shown in Fig. 9(c), 9(e) and 9(f). Hence, indirect load (deflection of the shell) has a significant effect on the fluid pressure.

4.4 Coup-Countercoup Effect. Coup-countercoup effect is common in blunt impacts that are primarily due to the relative motion of the skull and the brain [47–49]. However, Coup-countercoup effect in BINT [17,21,29,50,51] may or may not be due to this relative motion, since head acceleration is significantly less, at least during the time point of our investigation (first 2.5 ms) [17].

Negative pressures are observed at the rear end (B2) of the fluid in the steel case and are absent in the polycarbonate case (Fig. 9). Thus, the present study clearly shows that the coup-countercoup effect in BINT is dictated by the wave propagation within the shell compared to that in the fluid as shown in Fig. 1(e), and not by global acceleration/deceleration effects. This is explained with the help of simulations. Figure 12 shows the pressure/stress waves in the fluid/shell for both 2 mm polycarbonate and steel cases at various time points of interest; here the latter shows the counter-coup effect while the former does not. In steel case, compressive stress waves generated in the shell at the blast impinging region (F1) travel along the shell (F1-M1-B1) and transmits tensile (expansion) wave to the fluid near B2. Stress wave velocity in steel is approximately four times higher than that in the fluid, and hence produces countercoup effect. In polycarbonate case, the time taken by the stress waves to travel along the circumference (F1-M1-B1) of the shell is longer than the time taken by the pressure wave (F2) in the fluid to travel across the cylinder (F2-M2-B2); hence there is no countercoup effect. Thus, indirect load can induce negative pressures (tension) when the acoustic velocity in the solid is much higher than that in the fluid.

4.5 Effect of Cylinder Radius. The 25 mm radius polycarbonate cylinder used in the experiments corresponds to the head of small animal (e.g., rodents) specimens that are frequently tested in BINT studies [16,26]. However, the applicability of this model to human head is not so obvious. For this reason, numerical analysis is conducted on a 75 mm radius polycarbonate cylinder (2 mm thick) subjected to similar blast loading conditions. Radius of 75 mm is reasonably similar to the average dimensions of a human head. Figure 13 shows the comparison of fluid pressure and shell strain between 25 mm and 75 mm cylinder radius cases. The pressure patterns for 75 mm cylinder at all locations (F2, M2 and B2) are similar to 25 mm cylinder. Deflection of the shell is less in 75 mm cylinder due to increase in the flexural rigidity; thus the deflection induced load (indirect load) reduces. Oscillations similar to that of 25 mm case are observed at the fluid center (M2), but
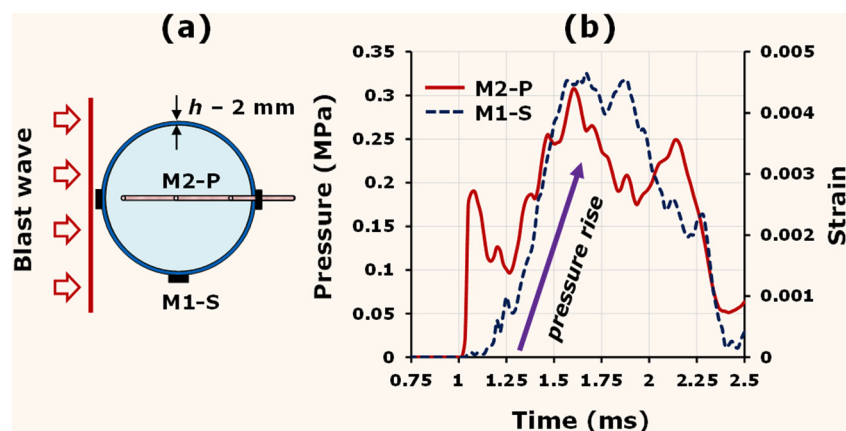

Fig. 11 Comparison of external deformation of the cylinder (strain at M1) and fluid pressure in M2 in 2 mm polycarbonate system: (*a*) Schematic; (*b*) Concurrent pressure rise in the fluid and strain indicating indirect load
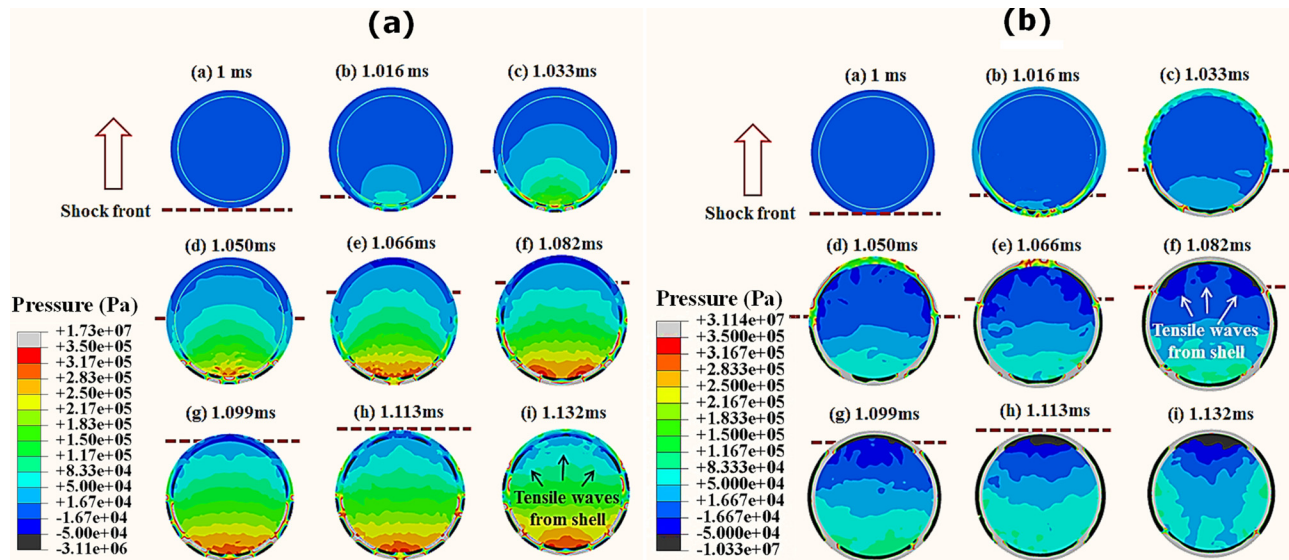
Fig. 12 Wave propagation in the cylindrical shell and the fluid at different time points with respect to the external shock front: (*a*) 2 mm polycarbonate cylinder (*b*) 2 mm steel cylinder
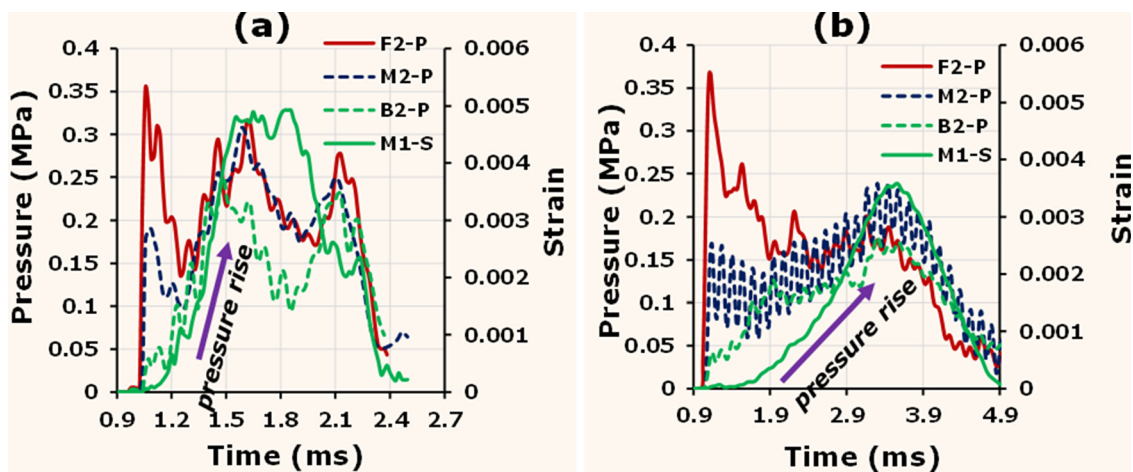

Fig. 13 Comparison of fluid pressures and external deformation (strain at M1) of the 2 mm polycarbonate cylinder (*a*) 25 mm radius cylinder (*b*) 75 mm radius cylinder

its frequency is different due to changes in wave propagation distance. Differences in oscillation frequencies are also seen between our experimental data on rat (r ∼ 15 mm) and PMHS (r ∼ 75 mm) [52,53]. The wave arrival times at F2, M2, and B2 for 75 mm cylinder yield the same acoustic velocity of fluid as that of 25 mm cylinder case. Hence, the results obtained for the 2 mm thick polycarbonate cylinder with 75 mm diameter can be applied to human head in terms of the loading path and pressure pulses in the fluid.

However, as the geometry of the human skull is much more complex with thickness varying from 2 mm to 7 mm, care should be exercised while applying these results.

Some of the limitations in this study are: (i) A fluid filled cylinder is used as a surrogate head; thus, all the results should be viewed in qualitative terms as response of human head will vary due to variations in geometry and materials. (ii) While studying the response of the fluid filled cylinder to the blast wave, we are

Table 3 Experimentally measured arrival times for 2 mm polycarbonate cylinder

	Blast overpressure			Fluid pressure			Shell strain		
	F1-P	M1-P	B1-P	F2-P	M2-P	B2-P	F1-S	M1-S	B1-S
Arrival time – t (µs)	1000	1046 ± 1	1138 ± 1.5	1006	1020 ± 0.95	1033 ± 0.49	1004	1021	1037 ± 0.58
Distance travelled by the waves – S (mm)	0	25	50	0	19	38	0	39.25	78.5
Velocity – dS/dt (m/s)	—	545 ± 10 (Blast wave – Air)	270 ± 5	—	1357 ± 100 (Pressure wave – Mineral oil)	1461 ± 60	—	2308 (Stress wave – Polycarbonate)	2453 ± 90

mainly focused on key parameters like peak pressure and the shape of the pressure pulse inside the fluid due to the blast wave. Thus, many aspects of blast physics like Mach reflection, flow field around the cylinder are not studied in great detail. The problem of shock wave interaction with the structure can be very complex depending upon nature of the problem (e.g., viscous versus inviscid fluids, boundary layer effects) and the goal of the research work. (iii) Only positive phase of the blast wave is considered in this work hence effects of negative phase on fluid pressure inside the cylindrical cavity are not studied. (iv) Mineral oil is used as brain simulant which is less susceptible to cavitation and hence cavitation effects are not studied in this work.

5   Conclusions

Blast induced neurotrauma has been recognized as the signature wound of the recent military conflicts. However, the dynamics of how the external blast load induces pressure/stress/strain in the brain is not well understood. This understanding is critical in assessing the blast injury response of the brain in order to protect, diagnose, treat and care for BINT. In this paper a fluid-filled cylinder is used as the surrogate for the head-brain complex and is subjected to a field-relevant blast load in a novel blast wave generator at UNL. Based on experimental and simulation study, the following conclusions can be made. They are:

- Blast flow field around the cylinder is governed by the geometry of the cylinder. The amplification factor $\wedge$ (ratio of reflected overpressure on the cylinder surface to that of far-field side-on incident pressure) is governed by the orientation of the cylinder with respect to the direction of blast wave propagation, and the dynamics of fluid-structure interaction. $\wedge$ is maximum in the frontal section and reduces in the middle and the posterior sections. Hence the loading in the frontal section greatly determines the biomechanical loading of the shell and the fluid.
- The total load at a point in the fluid can be partitioned into direct and indirect loads. Direct load is the stress wave transmitted from the blast to the cylinder and then to the fluid and is governed by the acoustic impedance mismatch. Higher the mismatch, lower is the transmission. Indirect load is the loading arising from the deflection of the container that loads the fluid, and this is governed by material stiffness and thickness of the shell. Higher the stiffness or/and the thickness, lesser is the indirect load.
- In case of deflection-dominated thin cylinders, the cylindrical shell changes its shape from a circular cross-section to elliptical and then restores back to a circular section. For thick cylinders the shape change is minimal. The shape change induces a rising pressure response in the fluid that is absent for thick cylinders.
- Pressure history in the fluid is governed by the interaction of multiple waves emanating from different points.
- In the ranges of air blast (field-relevant) load, peak pressure at any given point in the fluid is governed by the direct transmissive load. The duration of impulsive pressure load is governed by deflection-induced indirect loads.
- Based on the time difference in the stress wave propagation of the solid and the fluid, in some special cases, negative pressures can occur in the contrecoup region; this is indirect load and can possibly lead to cavitation in the fluid.

Acknowledgment

Nomenclature

p^* = blast wave peak overpressure
$p(t)$ = blast wave overpressure at time t
t^* = positive duration of blast wave
Ω = heterogeneous body ($\Omega_1 \cup \Omega_2$)
Ω_1 = homogenous shell medium
Ω_2 = homogenous fluid medium
h = shell thickness of Ω_1
S_1 = Sec. 1 in heterogeneous body
S_2 = Sec. 2 in heterogeneous body
S_3 = Sec. 3 in heterogeneous body
t_1 = time at which shock front interacts with S_1
t_2 = time at which shock front interacts with S_2
t_3 = time at which shock front interacts with S_3
$P_{\Omega2}$ = total load at any point in medium Ω_2
P_1 = load at any point in fluid Ω_2 from Sec. 1
P_2 = load at any point in fluid Ω_2 from Sec. 2
P_d = direct load (transmission from shell near blast wave interaction)
P_{id} = indirect load ($P_{id}^a + P_{id}^b$)
P_{id}^a = indirect load due to structural deflection of the shell
P_{id}^b = indirect load due to stress wave propagation in the unexposed region about Ω_1
$t_{1\text{-}d}$ = duration of direct load (P_d) from Sec. 1
$t_{1\text{-}id}^a$ = duration of indirect load (P_{id}^a) from Sec. 1
$t_{1\text{-}id}^b$ = duration of indirect load (P_{id}^b) from Sec. 1
$t_{2\text{-}d}$ = duration of direct load (P_d) from Sec. 2
$t_{2\text{-}id}^a$ = duration of indirect load (P_{id}^a) from Sec. 2
$t_{2\text{-}id}^b$ = duration of indirect load (P_{id}^b) from Sec. 2

References

[1] Courtney, A. C., and Courtney, M. W., 2009, "A Thoracic Mechanism of Mild Traumatic Brain Injury Due to Blast Pressure Waves," Med. Hypotheses, **72**(1), pp. 76–83.
[2] Cernak, I., Wang, Z., Jiang, J., Bian, X., and Savic, J., 2001, "Ultrastructural and Functional Characteristics of Blast Injury-Induced Neurotrauma," J. Trauma, **50**(4), pp. 695–706.
[3] Cernak, I., Savic, J., and Lazarov, A., 1997, "Relations Among Plasma Prolactin, Testosterone, and Injury Severity in War Casualties," World J. Surg., **21**(3), pp. 240–246.
[4] Cramer, F., Paster, S., and Stephenson, C., 1949, "Cerebral Injuries Due to Explosion Waves– 'Cerebral Blast Concussion' A Pathologic, Clinical and Electroencephalographic Study," Arch. Neurol., **61**(1), pp. 1–20.
[5] Young, M. W., 1945, "Mechanics of Blast Injuries," War Medicine, **8**(2), pp. 73–81.
[6] Stewart, O., Russel, C., and Cone, W., 1941, "Injury to the Central Nervous System by Blast," The Lancet, **237**(6128), pp. 172–174.
[7] Rafaels, K., Bass, C. R., Salzar, R. S., Panzer, M. B., Woods, W., Feldman, S., Cummings, T., and Capehart, B., 2011, "Survival Risk Assessment for Primary Blast Exposures to the Head," J. Neurotrauma, **28**(11), pp. 2319–2328.
[8] Cheng, J., Gu, J., Ma, Y., Yang, T., Kuang, Y., Li, B., and Kang, J., 2010, "Development of a Rat Model for Studying Blast-Induced Traumatic Brain Injury," J. Neurol. Sci., **294**(1–2), pp. 23–28.
[9] Long, J. B., Bentley, T. L., Wessner, K. A., Cerone, C., Sweeney, S., and Bauman, R. A., 2009, "Blast Overpressure in Rats: Recreating a Battlefield Injury in the Laboratory," J. Neurotrauma, **26**(6), pp. 827–840.
[10] Chavko, M., Koller, W. A., Prusaczyk, W. K., and Mccarron, R. M., 2007, "Measurement of Blast Wave by a Miniature Fiber Optic Pressure Transducer in the Rat Brain," J. Neurosci. Methods, **159**(2), pp. 277–281.
[11] Romba, J. J., and Martin, P., 1961, "The Propagation of Air Shock Waves on a Biophysical Model (No. TM-17-61)," Human Engineering Lab Aberdeen Proving Ground, Aberdeen, MD.
[12] Clemedson, C. J., and Pettersson, H., 1956, "Propagation of a High Explosive Air Shock Wave through Different Parts of an Animal Body," Am. J. Physiol., **184**(1), pp. 119–26.
[13] Clemedson, C. J., and Pettersson, H., 1953, "Genesis of Respiratory and Circulatory Changes in Blast Injury," Am. J. Physiol., **174**(2), pp. 316–320.
[14] Krohn, P., Whitteridge, D., and Zuckerman, S., 1941, "The Effect of Blast on the Heart and Head," UK Ministry of Home Security: Research and Experiments Department, Civil Defence Research Committee, Report HO, **195**(11), pp. 249.
[15] Dal Cengio Leonardi, A., Bir, C. A., Ritzel, D. V., and Vandevord, P. J., 2011, "Intracranial Pressure Increases During Exposure to a Shock Wave," J. Neurotrauma, **28**(1), pp. 85–94.

[16] Bolander, R., Mathie, B., Bir, C., Ritzel, D., and Vandevord, P., 2011, "Skull Flexure as a Contributing Factor in the Mechanism of Injury in the Rat When Exposed to a Shock Wave," Ann. Biomed. Eng., **39**(10), pp. 2550–2559.

[17] Moss, W. C., King, M. J., and Blackman, E. G., 2009, "Skull Flexure From Blast Waves: A Mechanism for Brain Injury With Implications for Helmet Design," Phys. Rev. Lett., **103**(10), pp. 108–702.

[18] Teasdale, G., and Jennett, B., 1974, "Assessment of Coma and Impaired Consciousness: A Practical Scale," The Lancet, **304**(7872), pp. 81–84.

[19] Chavko, M., Watanabe, T., Adeeb, S., Lankasky, J., Ahlers, S. T., and Mccarron, R. M., 2011, "Relationship Between Orientation to a Blast and Pressure Wave Propagation Inside the Rat Brain," J. Neurosci. Methods, **195**(1), pp. 61–66.

[20] Bir, C., 2011, "Measuring Blast-Related Intracranial Pressure Within the Human Head," Final Report, U.S. Army Medical Research and Material Command, Award No. W81XWH-09-1-0498.

[21] Zhu, F., Wagner, C., Dal Cengio Leonardi, A., Jin, X., Vandevord, P., Chou, C., Yang, K. H., and King, A. I., 2012, "Using a Gel/Plastic Surrogate to Study the Biomechanical Response of the Head Under Air Shock Loading: A Combined Experimental and Numerical Investigation," Biomech. Model. Mechanobiol., **11**(3–4), pp. 341–353.

[22] Varas, J. M., Philippens, M., Meijer, S., Van Den Berg, A., Sibma, P., Van Bree, J., and De Vries, D., 2011, "Physics of IED Blast Shock Tube Simulations for mTBI Research," Frontiers in Neurology, **2**(58).

[23] Alley, M. D., Schimizze, B. R., and Son, S. F., 2011, "Experimental Modeling of Explosive Blast-Related Traumatic Brain Injuries," NeuroImage, **54**(1), pp. S45–S54.

[24] Skotak, M., Wang, F., and Chandra, N., 2012, "An in vitro Injury Model for SH-SY5Y Neuroblastoma Cells: Effect of Strain and Strain Rate," J. Neurosci. Methods, **205**(1), pp. 159–168.

[25] Arun, P., Spadaro, J., John, J., Gharavi, R. B., Bentley, T. B., and Nambiar, M. P., 2011, "Studies on Blast Traumatic Brain Injury Using *In-Vitro* Model With Shock Tube," NeuroReport, **22**(8), pp. 379–384.

[26] Sundaramurthy, A., Alai, A., Ganpule, S., Holmberg, A., Plougonven, E., and Chandra, N., 2012, "Blast-Induced Biomechanical Loading of the Rat: An Experimental and Anatomically Accurate Computational Blast Injury Model," J. Neurotrauma, **29**(13), pp. 2352–2364.

[27] Kodama, T., Hamblin, M. R., and Doukas, A. G., 2000, "Cytoplasmic Molecular Delivery With Shock Waves: Importance of Impulse," Biophys. J., **79**(4), pp. 1821–1832.

[28] Suneson, A., Hansson, H. A., and Seeman, T., 1990, "Pressure Wave Injuries to the Nervous System Caused by High-Energy Missile Extremity Impact: Part I. Distant Effects on the Central Nervous System–A Light and Electron Microscopic Study on Pigs," J. Trauma, **30**(3), pp. 295–306.

[29] Taylor, P. A., and Ford, C. C., 2009, "Simulation of Blast-Induced Early-Time Intracranial Wave Physics Leading to Traumatic Brain Injury," ASME J. Biomech. Eng., **131**(6), p. 061007.

[30] Cullis, I. G., 2001, "Blast Waves and How They Interact With Structures," J.R. Army Med Corps, **147**(1), pp. 16–26.

[31] Zhang, L., Yang, K. H., and King, A. I., 2004, "A Proposed Injury Threshold for Mild Traumatic Brain Injury," ASME J. Biomech. Eng., **126**(2), pp. 226–236.

[32] Chen, X., and Chandra, N., 2004, "The Effect of Heterogeneity on Plane Wave Propagation Through Layered Composites," Compos. Sci. Technol., **64**(10–11), pp. 1477–1493.

[33] Chen, X., Chandra, N., and Rajendran, A. M., 2004, "Analytical Solution to the Plate Impact Problem of Layered Heterogeneous Material Systems," Int. J. Solids Struct., **41**(16–17), pp. 4635–4659.

[34] Rahman, M. A., and Rahman, A. S., eds., 2005, *Design Parameters of a Circular Proving Ring of Uniform Strength*, Proceedings of the International Conference on Mechanical Engineering 2005 (ICME2005), 28–30 December 2005, Dhaka, Bangladesh, pp. 1–5. Available at http://www.buet.ac.bd/me/icme/icme2005/Proceedings/PDF/ICME05-AM-15.pdf

[35] Chandra, N., Holmberg, A., and Feng, R., 2011, "Controlling the Shape of the Shock Wave Profile in a Blast Facility," US Provisional Patent Application, 61542354.

[36] Ganpule, S., Alai, A., Plougonven, E., and Chandra, N., 2012, "Mechanics of Blast Loading on the Head Models in the Study of Traumatic Brain Injury Using Experimental and Computational Approaches," Biomech. Model. Mechanobiol.

[37] Chandra, N., Ganpule, S., Kleinschmit, N., Feng, R., Holmberg, A., Sundaramurthy, A., Selvan, V., and Alai, A., 2012, "Evolution of Blast Wave Profiles in Simulated Air Blasts: Experiment and Computational Modeling," Shock Waves, **22**(5), pp. 403–415.

[38] Mowatt, S., and Skews, B., 2011, "Three Dimensional Shock Wave/Boundary Layer Interactions," Shock Waves, **21**(5), pp. 467–482.

[39] Ganpule, S., Gu, L., Alai, A., and Chandra, N., 2011, "Role of Helmet in the Mechanics of Shock Wave Propagation Under Blast Loading Conditions," Comput. Methods Biomech. Biomed. Eng., **15**(11), pp. 1–12.

[40] Chafi, M. S., Karami, G., and Ziejewski, M., 2009, "Numerical Analysis of Blast-Induced Wave Propagation Using Fsi and Alemulti-Material Formulations," Int. J. Impact Eng., **36**(10–11), pp. 1269–1275.

[41] Honma, H., Ishihara, M., Yoshimura, T., Maeno, K., and Morioka, T., 2003, "Interferometric Ct Measurement of Three-Dimensional Flow Phenomena on Shock Waves and Vortices Discharged From Open Ends," Shock Waves, **13**(3), pp. 179–190.

[42] Fry, F. J., and Barger, J. E., 1978, "Acoustical Properties of the Human Skull," J. Acoust. Soc. Am., **63**(5), pp. 1576–1590.

[43] Ludwig, G. D., 1950, "The Velocity of Sound Through Tissues and the Acoustic Impedance of Tissues," J. Acoust. Soc. Am., **22**(6), pp. 862–866.

[44] Carlucci, P., Mougeotte, C., Recchia, S., and Ji, H., 2010, "Novel Approach To Conducting Blast Load Analyses Using ABAQUS/Explicit-CEL," SIMULIA Customer Conference.

[45] Ofengeim, D. K., and Drikakis, D., 1997, "Simulation of Blast Wave Propagation Over a Cylinder," Shock Waves, **7**(5), pp. 305–317.

[46] Anderson, J. D., *Fundamentals of Aerodynamics* (McGraw-Hill, New York, 2001).

[47] Goggio, A. F., 1941, "The Mechanism of Contre-Coup Injury," J. Neurol., Neurosurg. Psychiatry, **4**(1), pp. 11–22.

[48] King, A. I., 2001, "Fundamentals of Impact Biomechanics: Part 2—Biomechanics of the Abdomen, Pelvis, and Lower Extremities," Annu. Rev. Biomed. Eng., **3**, pp. 27–55.

[49] Narayan Yoganandan, P. D., Frank, A., Pintar, P. D., and Sanford, J., Larson, M. D., Ph.D., *Frontiers in Head and Neck Trauma: Clinical and Biomechanical* (Medical College of Wisconsin, Milwaukee, 1998).

[50] Goeller, J., Wardlaw, A., Treichler, D., O'bruba, J., and Weiss, G., 2012, "Investigation of Cavitation as a Possible Traumatic Brain Injury (Tbi) Damage Mechanism From Blast," J. Neurotrauma, **29**(10), pp. 1970–1981.

[51] Tamer El Sayed, A. M., Fernando, F., and Michael, O., 2008, "Biomechanics of Traumatic Brain Injury," Comput. Methods Appl. Mech. Eng., **197**, pp. 4692–4701.

[52] Skotak, M., Wang, F., Alai, A., Holmberg, A., Harris, S., Switzer, R. C., III, and Chandra, N., 2013, "Rat Injury Model Under Controlled Field-Relevant Primary Blast Conditions: Acute Response to a Wide Range of Peak Overpressures," J. Neurotrauma, (in press).

[53] Ganpule, S., Alai, A., Salzar, R., and Chandra, N., 2013, "Intracranial Pressure Variations in a Post-Mortem Human Head Loaded by a Wide Range of Primary Blast Overpressures," (in press).